Experimental constraints on Mg isotope fractionation during clay formation: Implications for the global biogeochemical cycle of Mg

Ruth S. Hindshaw[a,1,*], Rebecca Tosca[b], Nicholas J. Tosca[b], Edward T. Tipper[a]

[a]*Department of Earth Sciences, University of Cambridge, Downing Street, Cambridge, CB2 3EQ, UK*
[b]*Department of Earth Sciences, University of Oxford, South Parks Road, Oxford, OX1 3AN, UK*

Abstract

The direction and magnitude of magnesium (Mg) isotope fractionation attendant to the formation of clay minerals is fundamental to the use of Mg isotopes to decipher the biogeochemical cycling of Mg in the critical zone and for the oceanic Mg budget. This study provides experimental data on the Mg fractionation factor for two smectite-group minerals (stevensite and saponite) at temperatures relevant for Earth surface processes. The resultant solids were characterised by X-ray diffraction (XRD) and Fourier-transform infrared spectroscopy (FT-IR) to confirm the mineralogy and crystallinity of the product. A series of experiments were performed to asses the impact of temperature and pH on isotope fractionation. Bulk solid samples were treated with ammonium chloride to remove exchangeable Mg in order to distinguish the Mg isotopic fractionation between these sites and octahedral sites.

All bulk and residual solids were enriched in ^{24}Mg compared to the initial solution and δ^{26}Mg values of the exchangeable pool were lower than, or within error of, the initial solution. Final solutions were either within error of, or enriched in, ^{26}Mg compared to the initial solution, depending on the fraction of Mg removed from solution (f_{Mg}). For experiments with small or negligible f_{Mg}, increasing the pH resulted in a higher reaction rate and reduced fractionation from the initial solution. This could point to a kinetic effect, but the composition of the residual solid (Mg/(Li+Mg) ratio) was also dependent on pH. The change in the composition was reflected in the wavenumber of the Mg$_3$-OH stretch in FT-IR data, which is a proxy for bond strength, and suggests an equilibrium control. An equilibrium control is further supported by the observation of reduced fractionation compared to the initial solution with increasing temperature. Rayleigh and batch fractionation models were fitted to the data giving fractionation factors of 0.9991 and 0.9990 respectively.

We compare our results with existing field and experimental data and suggest that the apparent contradictions surrounding the direction of Mg isotope fractionation into phyllosilicate minerals could be due to the similarity of Mg bond lengths between clay octahedral sites and dissolved Mg. Thus small changes in mineral structure or initial solution conditions may result in a change in bond length sufficient to alter the direction of fractionation, implying that the magnitude and direction of Mg isotope fractionation into clay minerals could be dependent on local field conditions. Alternatively, if the precipitation of secondary clay minerals in the field preferentially incorporates light Mg, as observed in this experimental study, this implies the contribution of carbonate weathering to dissolved Mg fluxes has been underestimated, with major implications for the global biogeochemical cycle of Mg.

1. Introduction

Magnesium (Mg) is the 8th most abundant mineral in the continental crust, 5th most abundant in the mantle and the 4th most abundant species in the hydrosphere (Teng, 2017). Further, Mg is an essential nutrient and plays a fundamental role in the carbon cycle via the sequestration of carbon dioxide in carbonate minerals (Berner et al., 1983). The global biogeochemical cycle of Mg represents one of the major transfers of mass on Earth between the lithosphere and hydrosphere via continental weathering and hydrothermal circulation (e.g. Lee et al., 2008). Clay minerals, which form in both the continental and marine realms, contain appreciable amounts of MgO (up to 35 wt%, e.g. Eberl et al., 1982) and several recent studies have highlighted the formation of marine clays as being key regulators of both the global cycle of Mg and the carbon cycle through reverse weathering processes (e.g. Higgins and Schrag, 2015; Isson and Planavsky, 2018).

In recent decades measurements of the stable isotope ratios of Mg ($^{26}Mg/^{24}Mg$ and $^{25}Mg/^{24}Mg$, reported as $\delta^{26}Mg$ and $\delta^{25}Mg$ in delta notation) have demonstrated that there is a $\sim$6‰ range in $\delta^{26}Mg$ values (Teng, 2017). This range is induced by low temperature dissolution-precipitation reactions that fractionate Mg isotopes such as the formation of secondary minerals e.g. carbonates and clays (Young and Galy, 2004). The distinct $\delta^{26}Mg$ values for different sample types has heralded the promise of using Mg isotopes to fingerprint the global biogeochemical cycle of Mg over geological time (e.g. Pogge von Strandmann et al., 2014; Higgins and Schrag, 2015; Dunlea et al., 2017). The key to applying Mg isotopes as a quantitative tracer of processes at scales from a single mineral to the entire planet is knowledge of the fractionation factors associated with the formation of secondary minerals. Studies of carbonates (low-Mg and high-Mg calcite, dolomite and magnesite) have all unambiguously demonstrated that they are enriched in the light isotope of Mg (^{24}Mg) relative to the starting solution (e.g. Pearce et al., 2012; Mavromatis et al., 2013; Schott et al., 2016; Oelkers et al., 2018).

In contrast, the direction of fractionation for clay minerals is not uniform. Whilst many field studies utilising Mg isotopes have suggested that clay minerals are enriched in the heavy isotope of Mg (^{26}Mg), the opposite sense of fractionation compared to carbonates (e.g. Teng et al., 2010; Schuessler et al., 2018), other field studies (e.g. Pogge von Strandmann et al., 2008; Ma et al., 2015; Gao et al., 2018b) have inferred that clays are enriched in the light isotope of Mg. In a clay mineral, there are at least two potential mineralogical sites for Mg, 1) structurally bound in octahedrally coordinated lattice sites and 2) loosely bound adsorbed or exchangeable sites associated with surface or interlayer negative charges (Meunier, 2005). Some field studies have been able to distinguish fractionation attendant

---

*corresponding author

Email address: `ruth.hindshaw@gmail.com` (Ruth S. Hindshaw)

[1]Present address: Norconsult AS, Kjørboveien 22, Sandvika, NO-1337

to each mineralogical site (Huang et al., 2012; Opfergelt et al., 2014). However, frequently in field studies the identity of the clay is not known and there is a fundamental ambiguity because of the potential dissolution and precipitation of carbonate minerals and/or atmospheric inputs to rivers and soils (e.g. Tipper et al., 2012).

Experimental studies of Mg isotope fractionation during clay mineral formation have focussed on analogue compounds with similar structure such as primary phyllosilicates and Mg hydroxide. To date, there are a handful of experimental syntheses in controlled laboratory conditions, but as with field studies, examples of preferential incorporation of both ^{24}Mg and ^{26}Mg have been reported (Li et al., 2014; Wimpenny et al., 2014; Ryu et al., 2016). Recent theoretical modelling studies predict that brucite should preferentially incorporate ^{26}Mg (Colla et al., 2018; Gao et al., 2018a; Wang et al., 2019), in agreement with experimental results at high (80°C) temperature (Wimpenny et al., 2014), but in contrast to the experimental results at low (<50°C) temperature (Li et al., 2014). Additional experimental data are required from well constrained laboratory studies to address the directionality and controls on Mg isotope isotope fractionation in clay minerals.

In the present study, we synthesised Mg-rich smectites common in the Earth surface environment at temperatures relevant to the critical zone and marine realm where reverse weathering and diagenesis occur. Our key finding is that the synthetic clays are enriched in the light isotope of Mg relative to the starting solution and that exchangeable and structurally bound Mg are fractionated to differing degrees. We discuss our data in the context of experimental variables (pH, temperature and solution composition), equilibrium and kinetic fractionation controls and explore the implications of our findings for the global biogeochemical cycle of Mg.

2. Materials and Methods

2.1. Investigated clay minerals

In this study two types of smectite were synthesised experimentally: stevensite and saponite. Smectites $((Na,Ca)_{0.3}(Al,Mg)_2Si_4O_{10}(OH)_2 \cdot nH_2O)$ are phyllosilicate minerals comprised of layers of octahedra (Mg/Al bonded to O or OH) sandwiched between two layers of Si tetrahedra (Si bonded to O or OH), referred to as 'TOT' or '2:1' clay minerals. Different clay minerals are defined based on the spacing between each TOT layer and their chemical composition. In some clay minerals, cation substitutions impart enough of a charge imbalance such that cations (including Mg) may be incorporated into these readily exchangeable interlayer sites, in addition to octahedral sites.

Stevensite is a trioctahedral smectite containing a Mg-rich octahedral sheet with vacancies and a Si-rich tetrahedral sheet (Guggenheim, 2016). Stevensite has an interlayer spacing (d_{001}) of ~14-15 Å. Octahedral vacancies (~0.08-0.10 cation sites per unit) are thought to give rise to an overall layer charge which imparts swelling characteristics and interlayer ion accommodation similar to other members of the smectite group (Brindley et al., 1977). Natural stevensite is often interstratified with a closely related, non-expandable phase called kerolite (Eberl et al., 1982). Kerolite exhibits a basal spacing commonly measured by powder X-ray diffraction (uncorrected for polarisation effects) of ~10.1 Å.

3

In this paper the term "stevensite" refers to this, rather than a pure stevensite end-member. Saponite has a similar structure to stevensite but with Al^{3+} substitution in both octahedral and tetrahedral sites.

These minerals commonly occur in association as direct precipitates from the weathering of ultramafic lithologies and during early diagenesis of marine and lacustrine sediments (e.g. Von Damm and Edmond, 1984). Since they exhibit relatively rapid reaction kinetics yet contain all of the essential structural characteristics of smectite and other TOT layer silicate minerals, the Mg-rich trioctahedral layer silicate minerals offer an ideal starting point for investigating low temperature clay mineral precipitation.

2.2. Clay synthesis

Mg-rich trioctahedral clays forming at low temperature in nature have an effective particle size of hundreds of nanometers and a low degree of crystallinity (Meunier, 2006). In order to target similar products we conducted experiments at low-temperature. Clay minerals were synthesised using two different methods and the two different clay minerals (stevensite and saponite) were targeted by adjusting the initial concentrations of Al in solution, as well as pH and temperature.

The first method used 1 L PPE bottles with an electrolyte buffer and the second method used a borosilicate glass reaction vessel coupled to an autotitrator. These two setups are hereafter referred to as 'bottle' and 'reaction vessel' experiments. Further details on the experimental conditions are reported in the Supplementary Information. Fourier Transform Infrared (FT-IR) spectroscopy and powder X-ray diffraction (XRD) were used to characterise the nature of the synthetic materials formed. Clay synthesis was conducted over a range of temperatures from 20 - 50°C (at constant pH), and a range of pH (at constant temperature) from 9.0 to 10.4 (Table S2). Aliquots of the initial and final solution were collected from all experiments and filtered at 0.22 μm. Solids from all experiments were recovered by filtration through 0.1 μm nitrocellulose filters. Part of the recovered clay sample was treated with ammonium chloride (1 M NH_4Cl) which will extract the Mg bound in exchangeable sites (Von Breymann and Suess, 1988). Both interlayer and adsorbed Mg are exchangeable and together these are referred to as the 'exchangeable phase'. The residue and an untreated bulk aliquot were digested in a mixture of concentrated HF and HNO_3.

2.3. Mg concentrations and isotope measurements

Mg concentration and isotope measurements were performed on digested solids (residual and bulk) and solutions (initial, final and supernatant of exchange procedure). Elemental concentrations were measured by inductively-coupled plasma optical emission spectrometry (ICP-OES, Agilent Technologies 5100, University of Cambridge) against synthetic calibration lines. Concentrations of the residual and exchangeable fractions are reported as mg Mg per kg of bulk sample. Average precision was better than 3% (RSD) as determined by repeat measurements of the Environment Canada certified reference materials TM-25.4 and BATTLE-02.

Mg isotopes were separated from matrix elements using the procedure described in Tipper et al. (2008). Magnesium isotope ratios were measured on a Neptune Plus multi-collector ICP-MS using an APEX IR sample introduction

system. ^{26}Mg/^{24}Mg and ^{25}Mg/^{24}Mg ratios were normalised to DSM3 using standard-sample bracketing (Galy et al., 2003). Analyses were performed on 100-200 ppb solutions using a 50 μL/min ESI PFA nebuliser with a typical beam size of 10 V on ^{24}Mg using medium resolution. Analyses of ^{26}Mg were conducted on a peak shoulder free of interferences. Accuracy and precision were monitored using several mono-elemental standards. Long-term reproducibility of DSM3 was 0.01±0.06‰ (2SD, n=19) and the values of the mono-elemental standards Cambridge-1, Paris-1 and Zürich-1 are in agreement with previously published values (Table S3). To ensure there was no fractionation induced during chemical separation, either seawater, a rock standard or a synthetic water standard (CCS2, Tipper et al., 2008) was processed with every batch of 5 samples (Table S3). The typical 2SD external reproducibility for δ^{26}Mg was 0.11‰. All of the Mg isotope data show mass dependent behaviour, defining a line with a gradient of 0.513±0.001 on a δ^{25}Mg′ vs δ^{26}Mg ′ plot (not shown). Due to variable δ^{26}Mg in the starting solutions, all data is reported as the difference between sample (x) and initial solution δ^{26}Mg values: Δ^{26}Mg = δ^{26}Mg$_x$ - δ^{26}Mg$_{init.-sln}$.

3. Results

3.1. Identity and crystallinity of solids precipitated

Transmission FT-IR and XRD spectra of the experiments targeting stevensite were described in Hindshaw et al. (2019). FT-IR spectra of all products were characterised by principal Si-O stretches ($\sim$1000-1020 cm^{-1}, Hindshaw et al., 2019) consistent with a 2:1 layer structure and Mg occupancy in trioctahedral sheets (Mg$_3$-OH stretch at 3680 cm^{-1}, Hindshaw et al., 2019). The spectra were also consistent with products which exhibited low crystallinity and small particle size (Figs. S7 and S8). Typical powder XRD peak positions were commonly located at either $\sim$10 Å or $\sim$14 Å for products from stevensite (Al-free) experiments (Table S4); samples in general were not responsive to ethylene glycol treatment (discussed in further detail in Hindshaw et al. (2019)). The range of XRD peak positions from 14 Å (stevensite) to 10 Å (kerolite) indicates that stevensite was mixed, and likely interstratified, with kerolite.

Powder XRD peak positions for products from saponite experiments indicate the solids were generally less crystalline, likely resulting from the presence of Al in the experiments. These data indicate that basal 001 reflections are not observable or very weak, which suggests that precipitates are largely 2-dimensional in nature and exhibit poor layer stacking order along the crystallographic c-axis. However, the position and relative intensity of powder XRD peaks from saponite experiments is consistent with a poorly crystalline layer silicate with a coherent scattering domain of $\sim$4 nm (Fig. S6). In addition, the composite reflection located at $\sim$1.53 Å indicates the presence of a trioctahedral sheet. FT-IR spectra of saponite products correspond closely with natural and synthetic saponite produced at higher temperatures (Farmer, 1974; Kloprogge and Frost, 2000). Specifically, these data further indicate that both Mg and Al are located in the layer silicate structure: typical FT-IR spectra yield lattice vibrations located at 469 and 755 cm^{-1} (arising from Al-OH translation and deformation modes, respectively) and 533 and 656 cm^{-1} (arising from Mg-OH perpendicular and libration modes, respectively; Fig. S7; Farmer, 1974; Kloprogge and Frost, 2000).
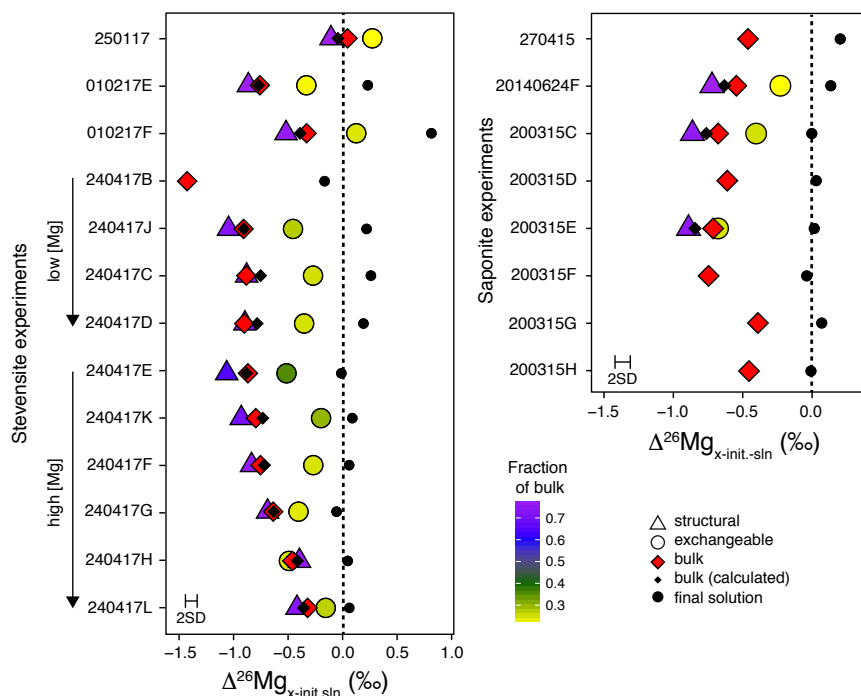
Figure 1: Summary of the Mg isotopic compositions for the exchangeable, residual, bulk and final solution phases for each of the experiments. All Mg isotopic compositions are plotted relative to the initial solution which is at 0‰ in this plot and highlighted by the dotted line. The calculated Δ^{26}Mg derived from mass balance is shown for comparison. The colour gradient of the exchangeable and residual Mg pools reflects the relative proportion of those pools to the bulk. The arrows for the high and low [Mg] series of experiments indicate increasing pH towards the head of the arrow. Left panel is for the stevensite (Al-free) experiments and the right panel is for the saponite (Al-containing) experiments. The 2SD experimental error (0.11‰) is comparable to the symbol size.

In addition to the targeted layer silicates, gibbsite was detected in experiments conducted at temperatures greater than 20°C (200315-G and 200315-H) and brucite was detected in the reaction vessel experiment 270415 (Fig. S6).

The experiments were not purged of carbon dioxide and therefore there is potential for carbonates to form which would fractionate Mg isotopes. However, the speciation of Mg in solution, calculated using PHREEQC, was >96.9% Mg^{2+} with the remainder $Mg(OH)^{+}$. There was negligible contribution from $MgCO_3$ in solution. In addition, we do not observe carbonate peaks in XRD or FT-IR spectra despite the analysis techniques employed being sensitive to carbonate (Fig. S8, Farmer, 1974), restricting the potential contribution of any carbonate to <1%.

3.2. Initial and final solutions

The Mg concentration of final solutions was lower than that of the initial solutions (Table 1). In the high [Mg] experiments the decrease in concentration was minor and the final solution δ^{26}Mg values were within error of the initial solution δ^{26}Mg values. In contrast, the decrease in [Mg] between the initial and final solution in experiments with low initial [Mg] (< 60 ppm) was marked. In one experiment (250117, Table 1), the [Mg] of the final solution was below the detection limit, consistent with the complete removal of Mg to secondary phases. In these low [Mg] experiments the final solution was enriched in ^{26}Mg compared to the initial solution by ~ 0.2‰ (Table 1, Fig 1).

6

3.3. Bulk solids, exchangeable and structural Mg

Bulk stevensite and saponite were enriched in ^{24}Mg (with mean δ^{26}Mg values of -0.68‰ for stevensite and -0.58‰ for saponite, compared to the initial solution), consistent with the final solutions being enriched in ^{26}Mg (Fig. 1, Table 1). For a given pH, solids precipitated from experiments with a high initial Mg concentration were less enriched in ^{24}Mg compared to those with low initial Mg (Fig. 2b).

Mg in bulk stevensite and saponite is a mixture of exchangeable (interlayer and adsorbed) Mg and structural (octahedral Mg). Exchangeable Mg comprised 17-33% of the bulk Mg whilst the residual solid contained 67-83% (Table 1, Fig. 1). Both the exchangeable pool and residual solids were enriched in ^{24}Mg compared to the initial solution, by 0.47 and 0.75‰ on average, respectively. The δ^{26}Mg values of the residual phases are lower than, or within error of, the bulk solid (Fig. 1, Table 1). The sum of exchangeable and residue mass weighted concentrations were within 8% of the measured bulk concentrations (excluding reaction vessel experiment 250117). Using the residual and exchangeable δ^{26}Mg values combined with the mass fractions of Mg, bulk δ^{26}Mg values were calculated and were within 0.13‰ of the measured bulk values, demonstrating the robustness and self consistency of the data. For all phases measured, the range of values measured in stevensite experiments overlapped with those measured in saponite experiments (Fig. 1).

^{7}Li-NMR data demonstrated that the cation exchange fractions contained up to 21% octahedral Li (Hindshaw et al., 2019). Modelling based on mass balance (see Supplementary Information) demonstrates that the exchangeable fraction cannot solely be comprised of octahedral Mg. Hence it is most likely that the enrichment of ^{24}Mg in the exchangeable Mg fraction is not an artefact of sample processing and represents a pool of Mg that is isotopically distinct from octahedral Mg.

3.4. Relationship between δ^{26}Mg and temperature

The temperature dependance of Mg isotope fractionation during the precipitation of saponite was investigated by conducting bottle experiments at pH 9 and with solutions of constant composition, but at variable temperatures of 20, 35 and 50°C (Table S2). Note that for these experiments, there was negligible depletion in the Mg content of the solutions (Table 1) meaning that any apparent temperature dependency cannot be the result of a mass balance effect.

There is a relationship between Δ^{26}Mg$_{residue-init.soln}$ and the inverse square of temperature (r^2=0.46, Fig. 2a) as would be expected for equilibrium isotope fractionation where apparent fractionation increases at lower temperatures (Schauble, 2004; Colla et al., 2018). The significance of this was further investigated using a Monte-Carlo simulation to take into account uncertainties in the measurements. The synthesised saponites were not treated with ammonium chloride to remove exchangeable Mg, which likely induces noise in the data. Additionally, gibbsite was detected in the experiments conducted at 35 and 50°C. Although gibbsite is not a Mg bearing mineral, it could impact solution δ^{26}Mg values if Mg were to adsorb onto it with isotopic fractionation.

Although the magnitude of fractionation observed in this study is greater than that observed by Li et al. (2014) for brucite precipitates treated to remove exchangeable Mg, the slopes of the two sets of data are indistinguishable
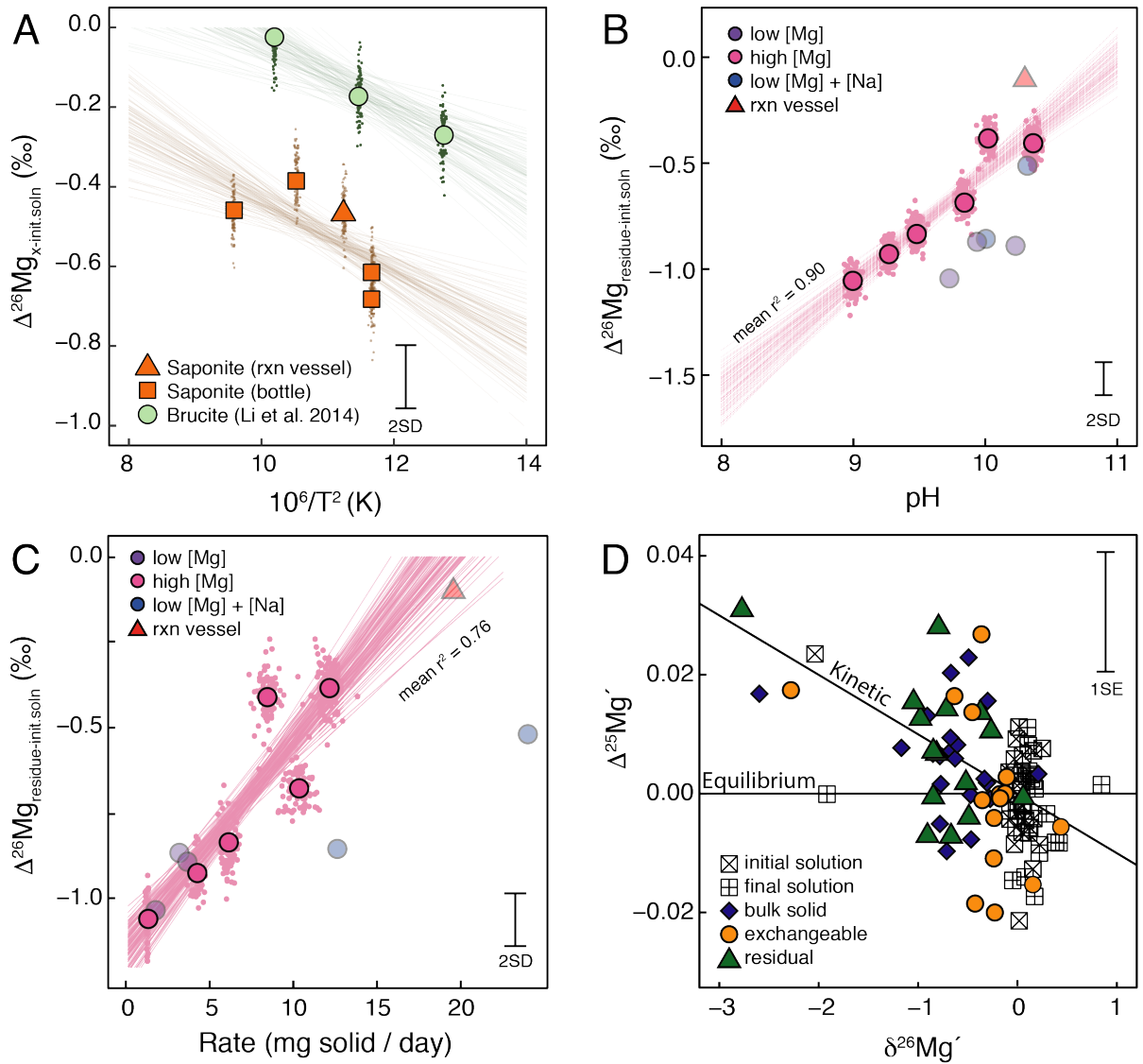
Figure 2: (A) Relationship between Δ^{26}Mg and the inverse of the temperature squared. The saponite samples are bulk solids whereas the brucite solids measured by Li et al. (2014) have been treated to remove exchangeable Mg. Relationship between Δ^{26}Mg and pH (B) and Δ^{26}Mg and reaction rate (C). A linear regression was fitted to the high [Mg] set of experiments red where there was negligible depletion of [Mg] from the initial solution. Data from the other stevensite experiments are shown as faded symbols for information. (D) Δ^{25}Mg′ vs δ^{26}Mg′. Δ^{25}Mg′ is defined as δ^{25}Mg′ $- 0.521\delta^{26}$Mg′ (Young and Galy, 2004) and values greater than zero are indicative of a component of kinetic fractionation. The 1SE error in δ^{26}Mg′ is smaller than the symbol size. In panels A-C Monte Carlo methods, which take into account measurement uncertainty, have been used to fit the data (n=1000). The clouds of points surrounding each primary data point represent individual simulations and each line indicates the best fit though one set of synthetic data.

₁₇₄ (-0.094±0.027 (1SD), Li et al. (2014); -0.095±0.027 (1SD), this study; Fig. 2).

₁₇₅ *3.5. Relationship between $\delta^{26}Mg$ and pH*

₁₇₆   The pH dependence of Mg isotope fraction during the precipitation of stevensite was investigated by conducting
₁₇₇ two series of bottle experiments at 20°C but variable pH from 9 to 10.4 (Table S2). One series was conducted at low
₁₇₈ [Mg] (2 mmol/kg) and the other at high [Mg] (20 mmol/kg) in the initial solution.

₁₇₉   For the bottle experiments conducted at 2 mmol/kg Mg, a significant fraction of Mg has been removed from the
₁₈₀ fluid by precipitation of the solid (Fig. 3) and therefore these experiments are dominated by a mass balance effect. In
₁₈₁ contrast, the maximum difference in $\delta^{26}Mg$ values between final and initial solutions for the experiments conducted
₁₈₂ at 20 mmol/kg Mg is < 0.10‰ (less than the analytical uncertainty). Whilst there are no clear relationships between
₁₈₃ either pH and bulk $\delta^{26}Mg$ values or pH and exchangeable $\delta^{26}Mg$ values (Fig. S9), there is a strong relationship
₁₈₄ between pH and residual $\delta^{26}Mg$ values (after ammonium chloride extraction, Fig. 2b), where at higher pH there is a
₁₈₅ smaller difference between the $\delta^{26}Mg$ value of the residue and the $\delta^{26}Mg$ value of the starting solution. There is also
₁₈₆ a relationship between the rate of precipitation (determined by the mass of solid recovered normalised to the number
₁₈₇ of days the experiment was conducted), pH and the $\delta^{26}Mg$ value of the residual solid (Fig. 2c).

₁₈₈ *3.6. Relationship between $\delta^{26}Mg$ and the chemical composition of the residue*

₁₈₉   For pairs of experiments conducted at similar pH, higher [Mg] is linked to reduced fractionation from the initial
₁₉₀ solution and lower Li/Mg values in the residual solid (Table 1). Within the high [Mg] series of experiments (constant
₁₉₁ starting solution but varying pH), higher pH was linked to an increase in the Mg/(Li+Mg) ratio of the residual solid
₁₉₂ (Fig. 4a).

₁₉₃ *3.7. Distinguishing between kinetic and equilibrium fractionation*

₁₉₄   Distinguishing between kinetic and equilibrium fractionation mechanisms is non trivial. In principle, it is possible
₁₉₅ to discriminate kinetic isotope fractionation from equilibrium isotope fractionation in stable isotope systems with
₁₉₆ more than two isotopes because of small differences in kinetic isotope fractionation between the two ratios; for Mg
₁₉₇ $^{26}Mg/^{24}Mg$ and $^{25}Mg/^{24}Mg$ (Young and Galy, 2004). These differences are usually expressed as $\Delta^{25}Mg'$, defined as
₁₉₈ $\delta^{25}Mg' - 0.521 \cdot \delta^{26}Mg'$, which describes the deviation from the equilibrium fractionation line (Table S5). Whilst
₁₉₉ there is a large uncertainty associated with $\Delta^{25}Mg'$ values, there is a significant difference between the $\Delta^{25}Mg'$ values
₂₀₀ of the initial solutions and the bulk solid products at 95% confidence value (Student's paired T-test), with the bulk
₂₀₁ solids having higher $\Delta^{25}Mg'$ values, consistent with at least a component of kinetic isotope fractionation (Fig. 2d).

₂₀₂ **4. Discussion**

₂₀₃   The most striking observation of the experimental data set is that the synthesised clay minerals are enriched in
₂₀₄ ^{24}Mg in both structural and exchangeable Mg and this is in contrast to some field and experimental observations. In
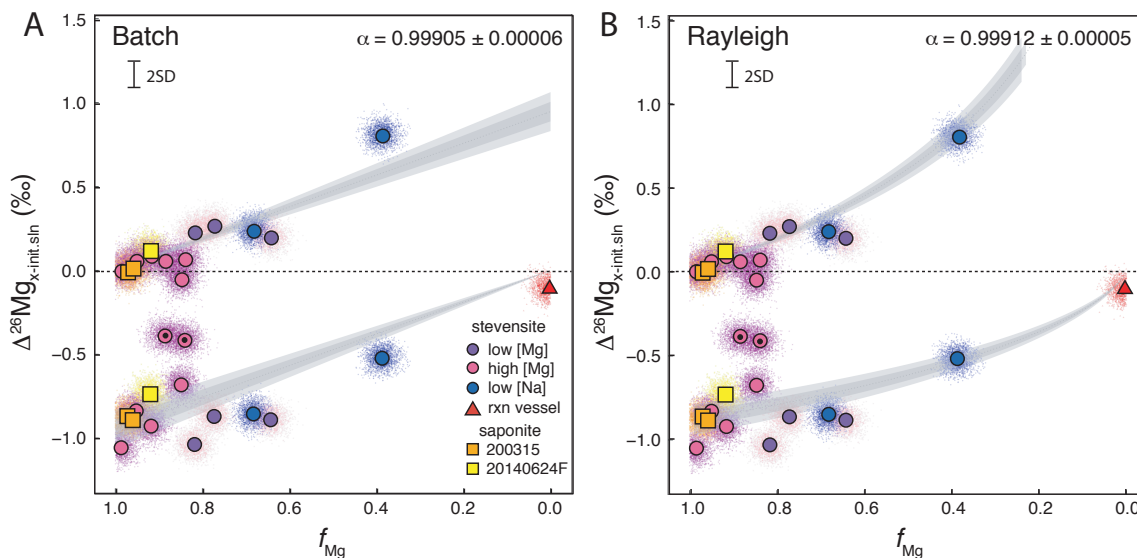
9

Figure 3: Mg isotope data of final solutions and residual solids (bulk solids treated to remove exchangeable Mg). f_{Mg} is calculated using the initial and final solution Mg concentrations. The data can be fitted by a batch (A) or Rayleigh (B) fractionation model (see Supplementary Information). Two of the high [Mg] bottle experiments (240417H and L, indicated with a black dot) are outliers in both models and this may be because additional factors, in addition to f_{Mg} are controlling the fractionation factor (see Fig. 4).

the following, the controlling factors on the observed Mg isotope fractionation are discussed and their implications for field studies explored.

4.1. Directionality of fractionation: Mg-O bond length

In isotopic equilibrium, the directionality of isotopic fractionation is predominantly set by the relative bond strength between the product and the reactant. The bond strength and frequency scale with bond length with strong bonds (high vibrational frequency), which favour the heavy isotope, being typically shorter (Bigeleisen, 1965). The fractionation in the present study is occurring between octahedrally coordinated Mg in structural sites in the synthetic clays and octahedrally coordinated Mg in an aquo complex where we assume there are two hydration shells ($[Mg(H_2O)_6](H_2O)_{12}^{2+}$). The ^{24}Mg enrichment in the residual solid (treated to remove exchangeable Mg) compared to the starting solution (Fig. 1) implies that the Mg–O bond in structural sites is longer than in aqueous Mg. This is supported by bond-length data indicating the the Mg–O bond in stevensite (2.085 Å, Table S6) is longer than in the aqueous species (2.072 Å, Table S6).

The ^{24}Mg enrichment observed in the exchangeable Mg fraction similarly implies longer Mg–O bonds in the exchange complex compared to Mg in solution. This would also be consistent with bond length data. Mg is likely bound in an outer-sphere complex (Meunier, 2005), with one layer of water molecules between the clay surface and the cation ($Mg(H_2O)_6^{2+}$). This species has a longer bond length of 2.08 Å compared to 2.07 Å for two hydration shells (Pavlov et al., 1998).

10

4.2. Kinetic versus equilibrium fractionation and estimation of fractionation factors

The relationship between the inverse square of temperature and apparent fractionation factor (R^2=0.46, Fig. 2a) could be indicative of equilibrium fractionation. The slope and hence the direction of fractionation is the same as that reported in Li et al. (2014) where a three-isotope method was employed to infer that equilibrium was reached. This method, however, is not possible when a solid is precipitated directly out of solution as in the present study.

To further evaluate the role of kinetic versus equilibrium fractionation, a batch and Rayleigh model were fitted through the stevensite and saponite data using a Monte-Carlo misfit method to determine the best-fit fractionation factor ($\alpha_{oct-water}$, Supplementary Information). Both the residues and final solutions can be fitted well with both a batch and a Rayleigh model (Fig. 3, Fig. S1) highlighting the difficulty of distinguishing equilibrium from kinetic effects. Most of residuals to the fits are < 0.2‰. However, there are two conspicuous outliers (Fig. 3, 240417H and L) to the trends. These two samples may have a different fractionation factor linked to the composition of the residual solid formed (Section 4.3). The best fit $\alpha_{oct-water}$ values were 0.99912 ± 0.00005 and 0.99905 ± 0.00006 for Rayleigh distillation and batch fractionation respectively. A contribution from both kinetic and equilibrium processes is consistent with the fact that the gradient of the best fit line in a plot of $\delta^{25}Mg'$ vs $\delta^{26}Mg'$ (0.513±0.001) lies between the theoretical slopes for kinetic fractionation (0.511) and equilibrium fractionation (0.521) (Young and Galy, 2004). If fractionation in a controlled laboratory setting can have a component of kinetic fractionation, then kinetic fractionation almost certainly occurs in field settings (Bouchez et al., 2013), and likely depends on fluid residence times and may occur via a diffusive mechanism with ^{24}Mg transported across mineral surfaces more efficiently than ^{26}Mg (Richter et al., 2008).

4.3. Effect of changing pH: reaction rate and compositional controls on fractionation factor

Although the data set can to a first approximation be fitted by a single fractionation factor (Fig. 3), there is variation in the high [Mg] series of experiments which results in two apparent outliers (240417H and L). The f_{Mg} of the high [Mg] series if experiments exhibits little variation (0.84 to 0.96) and there must therefore be additional, secondary, factors controlling fractionation. In this section we focus on the high [Mg] series of experiments.

An increase in pH can increase nucleation rate, growth rate and promotes better crystallisation. Therefore reaction rates should depend on pH and a kinetic effect on the apparent fractionation of Mg during experimental synthesis of minerals is common (e.g. Pearce et al., 2012; Mavromatis et al., 2013). In our data there is a relationship between reaction rate, pH and $\delta^{26}Mg$ for the high [Mg] series of experiments. However, we consider it unlikely that this relationship is caused by kinetic fractionation because the smallest isotopic fractionation is observed at the highest pH and reaction rate (Fig. 2b). This is opposite to that normally observed for kinetic fractionation where fractionation factors increase with increasing rate because of insufficient time for the back reaction (Nielsen et al., 2012).

Reaction rate is not the only variable dependent on pH. In addition, the elemental composition of the residual solids changes with pH. In the high [Mg] '240417' series of experiments the relative proportion of Li in the residual solid increases (Mg/(Li+Mg): 0.999984 to 0.999687) as pH decreases (10.36 to 8.99). Thus a change in composition

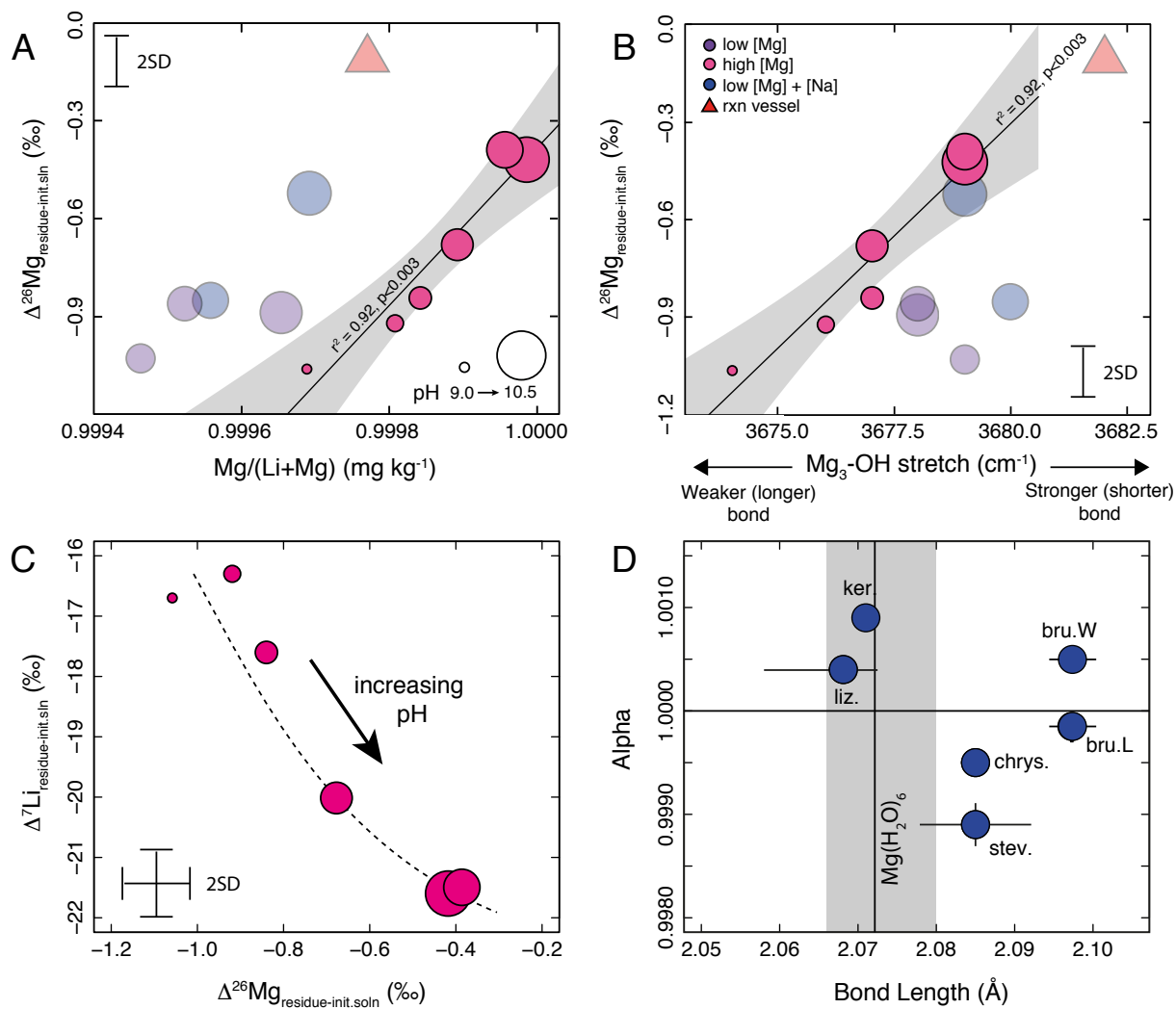Figure 4: (A) $\Delta^{26}Mg_{residue-init.sln}$ versus the Mg/(Li+Mg) ratio of the residual solid. (B) $\Delta^{26}Mg_{residue-init.sln}$ versus the wavenumber of the Mg$_3$-OH stretch in FT-IR spectra. For (A) and (B), a linear regression was fitted to the high [Mg] set of experiments. Data from the other stevensite experiments are shown as faded symbols for information. (C) Within the high [Mg] '240417' series there is an inverse relationship between $\Delta^{26}Mg_{residue-init.sln}$ and $\Delta^{7}Li_{residue-init.sln}$. In panels A-C, symbol size is scaled to pH. (D) Data on Mg fractionation factor and bond lengths for synthesised phyllosilicate minerals and brucite (Table S6). Literature sources: Kerolite (ker.) and Lizardite (liz.) - Ryu et al. (2016), Chysotile (chrys.) - Wimpenny et al. (2010), Brucite (bru.W) - Wimpenny et al. (2014), Brucite (bru.L) - Li et al. (2014), stevensite (stev.) - this study. When the Mg–O bond in the mineral is longer than that of the Mg-aquo complex, the mineral will be enriched in ^{24}Mg (e.g. brucite (bru.L), chrysotile, stevensite). Conversely, when the Mg–O bond in the mineral is shorter than in the Mg-aquo complex, the mineral will be enriched in ^{26}Mg (e.g. kerolite, lizardite).

may also contribute to the observed decrease in the magnitude of Mg isotope fractionation ($\Delta^{26}Mg_{residue-init.sln}$ -1.06 to -0.42) with increasing pH (Fig. 4a). The octahedral Mg bond length is determined by the chemical composition of the octahedral layer. A change in the relative proportion of two or more elements in the octahedral layer is predicted to affect isotope fractionation due to changes in bond lengths and vibrational frequencies (Wang et al., 2017) as the crystal structure distorts to accommodate an ion with a different charge and/or radius (Laurora et al., 2011; Michalski et al., 2015). For example, adding Mg to calcite ($CaCO_3$ to $(Mg_x,Ca_{1-x})CO_3$) causes the Mg–O bond length to change, directly impacting the fractionation factor (Wang et al., 2017) and increasing the Fe content of phyllosilicates was shown to increase the octahedral metal–O bond length (Laurora et al., 2011; Michalski et al., 2015).

We tested the extent to which the Li content of stevensite controls the Mg–O bond length by measuring the frequency of the Mg_3-OH stretch determined by FT-IR (Fig. 4b, Table S4). The position of the Mg_3-OH stretch is a function of bond length, electronegativity of the Mg-OH bond, the ionic and electric charge of Mg and OH and the coordination number. Within a controlled series of experiments (holding Mg, Na, Si, Al) constant, the latter three factors remain constant and therefore any variation should be solely due to bond length variations. A higher frequency stretch implies a stronger, shorter bond. For the high [Mg] '240417' series of bottle experiments, there is a positive relationship between the frequency of the Mg_3-OH stretch and $\Delta^{26}Mg$ values: fractionation increases as the Mg–O bond lengthens (Fig. 4b). The solids are enriched in ^{24}Mg compared to the starting solution (Fig. 1) implying that, in this case, the solid species has a longer bond compared to the aqueous species. Thus if the Mg–O bond in the solid increases in length, the difference between solid and aqueous species bond lengths will also increase, resulting in increased fractionation (Fig. 4d). Therefore the FT-IR data is consistent with an equilibrium control whereby adding Li into the octahedral layer increases the length of the Mg–O bond and increases the magnitude of the apparent fractionation factor (Fig. 4a,b). No such relationship exists for the low [Mg] series of experiments because of the mass balance effects on the data.

In a modelling study of the calcite-aragonite system a change from $CaCO_3$ to $(Mg_{0.5},Ca_{0.5})CO_3$ increased Ca–O bonds whilst Mg–O bonds decreased (Wang et al., 2017). Therefore we may expect a link between Mg–O and Li–O bond lengths. We do not have a direct measure of the Li–O bond length but this mechanism would be consistent with Li isotope data on the same sample set (Hindshaw et al., 2019). We observe that as the magnitude of Mg isotope fractionation decreases that of Li increases (Fig. 4c). This implies that as octahedral Mg–O bonds shorten (tend towards those in aqueous Mg, Fig. 4), Li-O octahedral bonds lengthen (tend away from those in aqueous Li). An equilibrium isotope fractionation mechanism could also account for the observation that increasing the proportion of Co in kerolite decreased the Mg fractionation factor (Ryu et al., 2016). The addition of Co could have changed the Mg-O bond length and thus the fractionation factor.

4.4. Comparison with existing experimental data

The clay minerals stevensite and saponite can be compared to existing literature data on primary phyllosilicates and brucite due to their similar structure. Based on recent experimental studies, Mg isotope fractionation into layer silicate

minerals and brucite is contradictory. Lizardite and kerolite have been shown to preferentially incorporate ^{26}Mg (Ryu et al., 2016), chrysotile ^{24}Mg (Wimpenny et al., 2010) and two experiments focussing on brucite precipitation reached opposite conclusions as to the direction of fractionation (Wimpenny et al., 2010; Li et al., 2014). Li et al. (2014) interpreted their data in terms of bond length controls on equilibrium isotope fractionation and in this section we interpret our data in the same way.

Literature data suggests that the average Mg–O bond lengths in phyllosilicate minerals kerolite and lizardite are shorter than the Mg–O bonds in the aquo complex (Table S6). These clays are correspondingly enriched in ^{26}Mg compared to the initial solution (Fig. 4d, Ryu et al., 2016). On the other hand, the average Mg–O bond in hectorite, chrysotile and brucite is longer than the aqueous Mg–O bond (Table S6) and these clays are enriched in ^{24}Mg (Fig. 4d, Wimpenny et al., 2010; Li et al., 2014). The one exception to this trend is the brucite experiments conducted by Wimpenny et al. (2014) where they found that ^{26}Mg was preferentially incorporated into the solid. The discrepancy between the direction of fractionation between Li et al. (2014) and Wimpenny et al. (2014) may be due to the different synthesis procedures employed. Li et al. (2014) reacted $MgO_{(s)}$ with 0.20 M $HCl_{(aq)}$ whereas Wimpenny et al. (2014) reacted 0.1 M $MgCl_{2(aq)}$ with 0.1M $NaOH_{(aq)}$. These differences may have resulted in non-identical Mg speciation in the reactants and products. The similarity in Mg–O bond length between Mg in an octahedral site in a phyllosilicate mineral and Mg in an aquo complex makes the directionality of Mg isotope fractionation sensitive to small changes in the Mg–O bond length and thus sensitive to the chemical structure and composition of the solid formed. The variable directionality of Mg isotope fractionation is worth contrasting with Li isotopes, where clays are always enriched in the light isotope ^{6}Li. For Li the hydrated complex is 4-fold coordinated ($Li(H_2O)_4$) and therefore has a very different bond length to an octahedrally coordinated site (1.9 vs 2.1 Å).

The sensitivity of Mg isotope fractionation to changes in phyllosilicate mineral structure is exemplified by comparing chrysotile and lizardite. Chrysotile and lizardite are two serpentine group minerals with the same chemical formula but differing crystal structures: lizardite is a 1:1 continuous layer silicate composed of a Mg-rich octahedral layer coordinated to a Si-rich tetrahedral layer, and chrysotile is a modulated 1:1 layer silicate featuring extensive curvature of the 1:1 sheets producing cylindrical or scroll-like structures. This affects the interlayer spacing and thickness of the octahedral sheet. These two parameters are greater in chrysotile compared to lizardite (Guggenheim, 2016), resulting in a longer Mg–O bond in chrysotile. In chrysotile the clay Mg–O bond is longer than aqueous Mg whereas in lizardite it is shorter. This results in these two phyllosilicate minerals having an opposite sense of fractionation to each other (Fig. 4d).

To date Mg isotope fractionation has only been investigated in trioctahedral phyllosilicate minerals, yet the dioctahedral phyllosilicate minerals such as montmorillonite and beidellite are more common in temperate weathering environments. Dioctahedral phyllosilicates only have 2/3 octahedral sites filled and this results in a smaller unit cell size (Meunier, 2005). Modelling results suggest that the Mg–O bond length in beidellite and dioctahedral smectites is less than 2 Å (Sainz-Díaz et al., 2001, 2002), which would result in the solid phase having a shorter bond length compared to the aqueous phase (Fig. 4d). Based on bond length we would therefore predict that dioctahedral

325 phyllosilicates would be enriched in ^{26}Mg, consistent with field data from temperate environments.

326 In summary, there appears to be a broad trend relating Mg–O bond length to the direction of Mg isotope fractionation. Further, the apparent sensitivity to bond length highlights the need to identify which clay minerals are forming at a given field site.

4.5. Implications for field studies

330 There are two key results from the present study that are pertinent to the interpretation of natural data. Firstly, the smectite mineral phases stevensite and saponite are enriched in ^{24}Mg, with an average fractionation factor (α) of 0.9990 (Table S6). The same isotopic enrichment has been observed for chrysotile and brucite (Wimpenny et al., 2010; Li et al., 2014). Secondly, exchangeable Mg is enriched in ^{24}Mg. The observation that river waters are nearly always enriched ^{24}Mg relative to silicate rocks has been interpreted to result from clays preferentially incorporating ^{26}Mg (Fig. 5, e.g. Tipper et al., 2006a; Bolou-Bi et al., 2012; Schuessler et al., 2018), an observation supported by some, but not all, measurements of bulk soils (Teng et al., 2010; Opfergelt et al., 2012; Schuessler et al., 2018). The direction of isotopic fractionation inferred from field data is opposite to the experimental data in the present study, prompting a series of questions for both experimental and field observations.

339 The inference that clay minerals preferentially incorporate ^{26}Mg in silicate catchments was largely based on the assumption that the chemical composition of natural waters is predominantly controlled by silicate mineral dissolution (e.g. Tipper et al., 2006a), requiring a mineral phase that preferentially retains ^{26}Mg in soil. However, even in silicate dominated catchments, trace carbonate can contribute significantly to riverine Mg (Wimpenny et al., 2011; Kimmig et al., 2018). Since carbonates are significantly enriched in ^{24}Mg relative to silicate rocks (Fig. 5), the preferential incorporation of ^{24}Mg into clay minerals from this source would result in river water enriched in ^{26}Mg relative to carbonate, but this water would appear enriched in ^{24}Mg relative to bulk silicate rock. This mechanism could reconcile the experimental results reported here with field observations. For example, the positive correlation observed between Li and Mg isotopes in river water samples from the Mackenzie Basin would be consistent with a common controlling mechanism: the formation of clay minerals (identity not determined) enriched in both ^{6}Li and ^{24}Mg, the light isotopes of Li of Mg.

350 Other processes may be important for specific field sites. The enrichment of ^{24}Mg in rivers compared to silicate rocks could be due to the preferential release of ^{24}Mg from primary minerals (Wimpenny et al., 2010; Maher et al., 2016). However, this hypothesis is likely only valid for the initial stages of weathering when the system is far from equilibrium and the enrichment of ^{24}Mg in rivers compared to silicate rocks has been observed in both weathering-limited and transport-limited field environments (Tipper et al., 2006b). In some field sites, ^{26}Mg-enriched soils has been attributed to sorption of Mg onto non-clay phases (e.g. gibbsite) and low-Mg clay minerals (e.g. kaolin minerals) rather than preferential uptake of ^{26}Mg into Mg-bearing clay minerals (Huang et al., 2012; Liu et al., 2014). Not all soils are enriched in ^{26}Mg (Fig. 5) and in these settings the enrichment of ^{24}Mg in soils compared to parent rock has been attributed to adsorption-desorption reactions, inputs from the atmosphere, biospheric cycling and the exchange
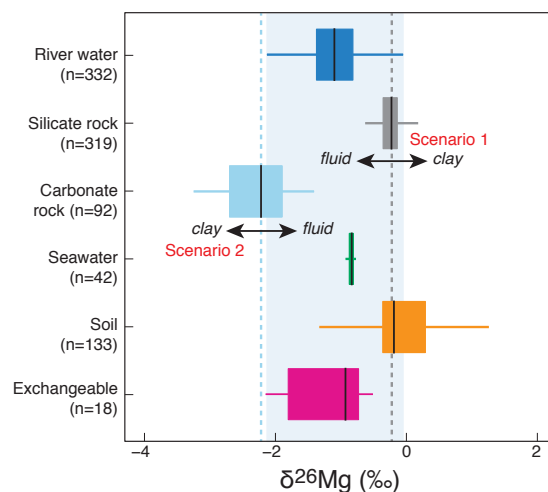
15

Figure 5: Mg isotope data from river water (n=332), silicate rock (n=319), carbonate rock (n=92), seawater (n=42), soil (n=133) and soil exchangeable Mg (n=18) compiled from field studies (see Supplementary Information for references). River water, seawater and soil exchangeable fluids have Mg isotopic compositions intermediate between carbonate and silicate rocks. The shaded area indicates the δ^{26}Mg range of river waters. The dashed lines indicate the mean δ^{26}Mg values for carbonate (light blue) and silicate (grey) rocks. Two fractionation scenarios are highlighted. In scenario 1, the initial solution is derived from silicate rocks. Secondary clays preferentially incorporate ^{26}Mg resulting in rivers enriched in ^{24}Mg relative to silicate rocks. In scenario 2 the initial solution is derived from carbonate rocks. Secondary clays preferentially incorporate ^{24}Mg resulting in rivers enriched in ^{26}Mg relative to carbonate rocks.

359 pool (e.g. Pogge von Strandmann et al., 2012; Opfergelt et al., 2014; Ma et al., 2015; Gao et al., 2018b). The presence

360 of organic chelates (Li et al., 2014) and bacteria (Oelkers et al., 2015; Balland-Bolou-Bi et al., 2019) can also affect the

361 magnitude and direction of Mg isotope fractionation. Whilst in natural systems the controls on the exchange pool are

362 myriad (adsorption, sea spray, litter decomposition etc.), and not solely due to secondary mineral formation (Opfergelt

363 et al., 2014), our data supports field evidence that the soil exchange pool has an affinity for ^{24}Mg (Gao et al., 2018b).

364   If the formation of clay minerals in natural settings results in the preferential incorporation of ^{24}Mg as reported in

365 this study, but contrary to previous interpretations based on field data (Tipper et al., 2006a), then it would have major

366 implications for the source of Mg to the hydrosphere in the global biogeochemical cycle of Mg. If this hypothesis is

367 correct, the intermediate δ^{26}Mg of seawater between carbonate and silicate sources (Fig. 5) could reflect a much more

368 significant input of Mg derived from carbonates than was previously considered. The implication is that carbonate

369 weathering may play a much more significant role in the global biogeochemical cycle of Mg with implications for

370 the carbon cycle since carbonate weathering is either CO_2 neutral or releases CO_2 depending on the weathering agent

371 (Calmels et al., 2007).

372   Finally, as alluded to in Section 4.4, the direction of fractionation may be dependent on the clay mineral structure.

373 A simple explanation for the discrepancy between field and experimental data would be that clays in question are dif-

374 ferent and therefore not directly comparable. Until the direction and magnitude of fractionation attendant to a greater

375 variety of clay types has been determined with greater certainty, interpretations of field data and the global biogeo-

376 chemical cycle of Mg will have an inherent ambiguity, highlighting the urgent need for additional field, experimental

377 and modelling studies.

16

5. Conclusions

We have synthesised Mg-rich layer silicate minerals at temperatures relevant for Earth surface processes, characterising the mineralogy, structure and Mg isotopic composition. Both stevensite and saponite were enriched in ^{24}Mg in the bulk and residual phases, relative to the initial solution. The exchangeable phase had δ^{26}Mg values lower than, or within error of, the initial solution. Due to the range in the fraction of Mg removed from the initial solution, a fractionation factor could be calculated using a batch and a Rayleigh model. Both models fit the data well with similar fractionation factors of 0.9990 (batch) and 0.9991 (Rayleigh).

Saponite was synthesised at a range of temperatures from 20-50°C. Fractionation decreased as temperature increased, in agreement with equilibrium fractionation. Interestingly, although the magnitude of fractionation was different, the direction of fractionation and relationship with temperature was similar to that observed for the fractionation of brucite over a similar temperature range (Li et al., 2014). Stevensite was synthesised over a range of pH values. Increased pH resulted in decreased fractionation relative to the initial solution. Although the reaction rate increased with pH, suggesting a kinetic effect, we argue this is not the case because 1) smaller fractionations are observed for greater reaction rates and 2) the composition of the product also changed. The wavenumber of the Mg_3-OH stretch in FT-IR spectra is a proxy for the octahedral Mg–O bond length and this data indicates that the octahedral bond length decreased with increasing pH, suggesting an equilibrium control.

To date, experimental studies of Mg isotope fractionation into clay minerals have appeared contradictory, with separate studies indicating that both heavy and light Mg can be incorporated into clay minerals. Unlike other metal cations, such as Li, the octahedral Mg–O bond length is similar to that of Mg in the initial solution (assumed to be an aquo-complex in these laboratory experiments). Small changes in structure between clay types determine whether the octahedral bond is longer or shorter compared to the initial solution, with implications for the directionality of the observed Mg fractionation factor. Our experimental data suggests that two Mg-layer silicate minerals, stevensite and saponite, preferentially incorporate ^{24}Mg. This questions the interpretation of some field studies which have suggested that secondary minerals preferentially incorporate ^{26}Mg. Either carbonate weathering is a more significant source of dissolved Mg than previously assumed or the similarity in bond length between Mg in clay minerals and Mg in an aquo-complex (or other solute Mg species) means that the dominant sense of fractionation in the field is different to that observed in this and other experimental studies. If the direction of fractionation in nature is the same as the present study, then the global biogeochemical cycle of Mg will need to be significantly revised.

6. Acknowledgments

17

7. References

Balland-Bolou-Bi, C., Bolou-Bi, E. B., Vigier, N., Mustin, C., Poszwa, A., 2019. Increased Mg release rates and related Mg isotopic signatures during bacteria-phlogopite interactions. Chem. Geol. 506, 17–28.

Berner, R. A., Lasaga, A. C., Garrels, R. M., 1983. The carbonate-silicate geochemical cycle and its effect on atmospheric carbon dioxide over the past 100 million years. Am. J. Sci. 283, 641–683.

Bigeleisen, J., 1965. Chemistry of isotopes. Science 147, 463–471.

Bolou-Bi, E. B., Vigier, N., Poszwa, A., Boudot, J.-P., Dambrine, E., 2012. Effects of biogeochemical processes on magnesium isotope variations in a forested catchment in the Vosges Mountains (France). Geochim. Cosmochim. Acta 87, 341–355.

Bouchez, J., von Blanckenburg, F., Schuessler, J. A., 2013. Modeling novel stable isotope ratios in the weathering zone. Am. J. Sci. 313, 267–308.

Brindley, G. W., Bish, D. L., Wan, H.-M., 1977. The nature of kerolite, its relation to talc and stevensite. Miner. Mag. 41, 443–452.

Calmels, D., Gaillardet, J., France-Lanord, C., 2007. Sustained sulfide oxidation by physical erosion processes in the Mackenzie River basin: Climatic perspectives. Geology 35, 1003–1006.

Colla, C. A., Casey, W. H., Ohlin, C. A., 2018. Computational prediction of Mg-isotope fractionation between aqueous $[Mg(OH_2)_6]^{2+}$ and brucite. Geochim. Cosmochim. Acta 227, 64–74.

Dunlea, A. G., Murray, R. W., Santiago Ramos, D. P., Higgins, J. A., 2017. Cenozoic global cooling and increased seawater Mg/Ca via reduced reverse weathering. Nat. Comm. 8, 844.

Eberl, D. D., Jones, B. F., Khoury, H. N., 1982. Mixed-layer kerolite/stevensite from the Amargosa Desert, Nevada. Clay Clay Miner. 30, 321–326.

Farmer, V. C., 1974. The layer silicates. In: The Infrared Spectra of Minerals. Vol. 4. Mineralogical Society of Great Britain and Ireland, London, UK, pp. 331–363.

Galy, A., Yoffe, O., Janney, P. E., Williams, R. W., Cloquet, C., Alard, O., Halicz, L., Wadhwa, M., Hutcheon, I. D., Ramon, E., Carignan, J., 2003. Magnesium isotope heterogeneity of the isotopic standard SRM980 and new reference materials for magnesium-isotope-ratio measurements. J. Anal. At. Spectom. 18, 1352–1356.

Gao, C., Cao, X., Liu, Q., Yang, Y., Zhang, S., He, Y., Tang, M., Liu, Y., 2018a. Theoretical calculation of equilibrium Mg isotope fractionations between minerals and aqueous solutions. Chem. Geol. 488, 62–75.

Gao, T., Ke, S., Wang, S.-J., Li, F., Liu, C., Lei, J., Liao, C., Wu, F., 2018b. Contrasting Mg isotopic compositions between Fe-Mn nodules and surrounding soils: Accumulation of light Mg isotopes by Mg-depleted clay minerals and Fe oxides. Geochim. Cosmochim. Acta 237, 205–222.

Guggenheim, S., 2016. Introduction to Mg-rich clay minerals: Structure and composition. In: Pozo, M., Galán, E. (Eds.), Magnesian clays: Characterization, origins and applications. No. 2 in AIPEA Educational Series. AIPEA, Bari, Italy, pp. 1–62.

Higgins, J. A., Schrag, D. P., 2015. The Mg isotopic composition of Cenozoic seawater - evidence for a link between Mg-clays, seawater Mg/Ca, and climate. Earth Planet. Sci. Lett. 416, 73–81.

Hindshaw, R. S., Tosca, R., Goût, T. L., Farnan, I., Tosca, N. J., Tipper, E. T., 2019. Experimental constraints on Li isotope fractionation during clay formation. Geochim. Cosmochim. Acta 250, 219–237.

Huang, K.-J., Teng, F.-Z., Wei, G.-J., Ma, J.-L., Bao, Z.-Y., 2012. Adsorption- and desorption-controlled magnesium isotope fractionation during extreme weathering of basalt in Hainan Island, China. Earth Planet. Sci. Lett. 359-360, 73–83.

Isson, T. T., Planavsky, N. J., 2018. Reverse weathering as a long-term stabilizer of marine pH and planetary climate. Nature 560, 471–475.

Kimmig, S. R., Holmden, C., Bélanger, N., 2018. Biogeochemical cycling of Mg and its isotopes in a sugar maple forest in Québec. Geochim. Cosmochim. Acta 230, 60–82.

Kloprogge, J. T., Frost, R. L., 2000. The effect of synthesis temperature on the FT-Raman and FT-IR spectra of saponites. Vib. Spectrosc. 23, 119–127.

Laurora, A., Brigatti, M. F., Malferrari, D., Galli, E., Rossi, A., 2011. The crystal chemistry of lizardite-1*T* from northern Apennines ophiolites near Modena, Italy. The Canad. Mineral. 49, 1045–1054.

Lee, C.-T. A., Morton, D. M., Little, M. G., Kistler, R., Horodyskyj, U. N., Leeman, W. P., Agranier, A., 2008. Regulating continent growth and composition by chemical weathering. P. Natl. Acad. Sci. 105, 4981–4986.

453 Li, W., Beard, B. L., Li, C., Johnson, C. M., 2014. Magnesium isotope fractionation between brucite [Mg(OH)$_2$] and Mg aqueous species:
454   Implications for silicate weathering and biogeochemical processes. Earth Planet. Sci. Lett. 394, 82–93.

455 Liu, X.-M., Teng, F.-Z., Rudnick, R. L., McDonough, W. F., Cummings, M. L., 2014. Massive magnesium depletion and isotope fractionation in
456   weathered basalts. Geochim. Cosmochim. Acta 135, 336–349.

457 Ma, L., Teng, F.-Z., Jin, L., Ke, S., Yang, W., Gu, H.-O., Brantley, S. L., 2015. Magnesium isotope fractionation during shale weathering in the
458   Shale Hills Critical Zone Observatory: accumulation of light Mg isotopes in soils by clay mineral transformation. Chem. Geol. 397, 37–50.

459 Maher, K., Johnson, N. C., Jackson, A., Lammers, L. N., Torchinsky, A. B., Weaver, K. L., Bird, D. K., Brown Jr., G. E., 2016. A spatially resolved
460   surface kinetic model for forsterite dissolution. Geochim. Cosmochim. Acta 174, 313–334.

461 Mavromatis, V., Gautier, Q., Bosc, O., Schott, J., 2013. Kinetics of Mg partition and Mg stable isotope fractionation during its incorporation in
462   calcite. Geochim. Cosmochim. Acta 114, 188–203.

463 Meunier, A., 2005. Clays. Springer-Verlag, Berlin, Germany.

464 Meunier, A., 2006. Why are clay minerals small? Clay Miner. 41, 551–566.

465 Michalski, J. R., Cuadros, J., Bishop, J. L., Dyar, M. D., Dekov, V., Fiore, S., 2015. Constraints on the crystal-chemistry of Fe/Mg-rich smectitic
466   clays on Mars and links to global alteration trends. Earth Planet. Sci. Lett. 427, 215–225.

467 Nielsen, L. C., DePaolo, D. J., De Yoreo, J. J., 2012. Self-consistent ion-by-ion growth model for kinetic isotopic fractionation during calcite
468   precipitation. Geochim. Cosmochim. Acta 86, 166–181.

469 Oelkers, E. H., Benning, L. G., Lutz, S., Mavromatis, V., Pearce, C. R., Plümper, O., 2015. The efficient long-term inhibition of forsterite dissolution
470   by common soil bacteria and fungi at Earth surface conditions. Geochim. Cosmochim. Acta 168, 222–235.

471 Oelkers, E. H., Berninger, U.-N., Pérez-Fernàndez, A., Chmeleff, J., Mavromatis, V., 2018. The temporal evolution of magnesium isotope fraction-
472   ation during hydromagnesite dissolution, precipitation, and at equilibrium. Geochim. Cosmochim. Acta 226, 36–49.

473 Opfergelt, S., Burton, K. W., Georg, R. B., West, A. J., Guicharnaud, R. A., Sigfusson, B., Siebert, C., Gislason, S. R., Halliday, A. N., 2014.
474   Magnesium retention on the soil exchange complex controlling Mg isotope variations in soils, soil solutions and vegetation in volcanic soils,
475   Iceland. Geochim. Cosmochim. Acta 125, 110–130.

476 Opfergelt, S., Georg, R. B., Delvaux, B., Cabidoche, Y.-M., Burton, K. W., Halliday, A. N., 2012. Mechanisms of magnesium isotope fractionation
477   in volcanic soil weathering sequences, Guadeloupe. Earth Planet. Sci. Lett. 341-344, 176–185.

478 Pavlov, M., Siegbahn, P. E. M., Sandström, M., 1998. Hydration of beryllium, magnesium, calcium, and zinc ions using density functional theory.
479   J. Phys. Chem. A 102, 219–228.

480 Pearce, C. R., Saldi, G. D., Schott, J., Oelkers, E. H., 2012. Isotopic fractionation during congruent dissolution, precipitation and at equilibrium:
481   Evidence from Mg isotopes. Geochim. Cosmochim. Acta 92, 170–183.

482 Pogge von Strandmann, P. A. E., Burton, K. W., James, R. H., van Calsteren, P., Gíslason, S. R., Sigfússon, B., 2008. The influence of weathering
483   processes on riverine magnesium isotopes in a basaltic terrain. Earth Planet. Sci. Lett. 276, 187–197.

484 Pogge von Strandmann, P. A. E., Opfergelt, S., Lai, Y.-J., Sigfússon, B., Gislason, S. R., Burton, K. W., 2012. Lithium, magnesium and silicon
485   isotope behaviour accompanying weathering in a basaltic soil and pore water profile in Iceland. Earth Planet. Sci. Lett. 339-340, 11–23.

486 Pogge von Strandmann, P. A. E., Porcelli, D., James, R. H., van Calsteren, P., Schaefer, B., Cartwright, I., Reynolds, B. C., Burton, K. W., 2014.
487   Chemical weathering processes in the Great Artesian Basin: Evidence from lithium and silicon isotopes. Earth Planet. Sci. Lett. 406, 24–36.

488 Richter, F. M., Watson, E. B., Mendybaev, R. A., Teng, F.-Z., Janney, P. E., 2008. Magnesium isotope fractionation in silicate melts by chemical
489   and thermal diffusion. Geochim. Cosmochim. Acta 72, 206–220.

490 Ryu, J.-S., Vigier, N., Decarreau, A., Lee, S.-W., Lee, K.-S., Song, H., Petit, S., 2016. Experimental investigation of Mg isotope fractionation
491   during mineral dissolution and clay formation. Chem. Geol. 445, 135–145.

492 Sainz-Díaz, C. I., Hernández-Laguna, A., Dove, M. T., 2001. Modeling of dioctahedral 2:1 phyllosilicates by means of transferable empirical
493   potentials. Phys. Chem. Minerals 28, 130–141.

494 Sainz-Díaz, C. I., Timon, V., Botella, V., Artacho, E., Hernández-Laguna, A., 2002. Quantum mechanical calculations of dioctahedral 2:1 phyl-
495   losilicates: Effect of octahedral cation distributions in pyrophyllite, illite, and smectite. Am. Mineral. 87, 958–965.

19

Schauble, E. A., 2004. Applying stable isotope fractionation theory to new systems. In: Johnson, C. M., Beard, B. L., Albarède, F. (Eds.), Geochemistry of Non-traditional Stable Isotopes. Vol. 55 of Reviews in Mineralogy & Geochemistry. Mineralogical Society of America, Washington, DC, pp. 65–111.

Schott, J., Mavromatis, V., Fujii, T., Pearce, C. R., Oelkers, E. H., 2016. The control of carbonate mineral Mg isotope composition by aqueous speciation: Theoretical and experimental modeling. Chem. Geol. 445, 120–134.

Schuessler, J. A., von Blanckenburg, F., Bouchez, J., Uhlig, D., Hewawasam, T., 2018. Nutrient cycling in a tropical montane rainforest under a supply-limited weathering regime traced by elemental mass balances and Mg stable isotopes. Chem. Geol. 497, 74–87.

Teng, F.-Z., 2017. Magnesium isotope geochemistry. In: Reviews in Mineralogy & Geochemistry. Vol. 82. Mineralogical Society of America, pp. 219–287.

Teng, F.-Z., Li, W.-Y., Rudnick, R. L., Gardner, L. R., 2010. Contrasting lithium and magnesium isotope fractionation during continental weathering. Earth Planet. Sci. Lett. 300, 63–71.

Tipper, E. T., Calmels, D., Gaillardet, J., Louvat, P., Capmas, F., Dubacq, B., 2012. Positive correlation between Li and Mg isotope ratios in the river waters of the Mackenzie Basin challenges the interpretation of apparent isotopic fractionation during weathering. Earth Planet. Sci. Lett. 333-334, 35–45.

Tipper, E. T., Galy, A., Bickle, M. J., 2006a. Riverine evidence for a fractionated reservoir of Ca and Mg on the continents: Implications for the oceanic Ca cycle. Earth Planet. Sci. Lett. 247, 267–279.

Tipper, E. T., Galy, A., Gaillardet, J., Bickle, M. J., Elderfield, H., Carder, E. A., 2006b. The magnesium isotope budget of the modern ocean: Constraints from riverine magnesium isotope ratios. Earth Planet. Sci. Lett. 250, 241–253.

Tipper, E. T., Louvat, P., Capmas, F., Galy, A., Gaillardet, J., 2008. Accuracy of stable Mg and Ca isotope data obtained by MC-ICP-MS using the standard addition method. Chem. Geol. 257, 65–75.

Von Breymann, M. T., Suess, E., 1988. Magnesium in the marine sedimentary environment: Mg-nh$_4$ ion exchange. Chem. Geol. 70, 359–371.

Von Damm, K. L., Edmond, J. M., 1984. Reverse weathering in the closed-basin lakes of the Ethiopian Rift. Am. J. Sci. 284, 835–862.

Wang, W., Qin, T., Zhou, C., Huang, S., Wu, Z., Huang, F., 2017. Concentration effect on equilibrium fractionation of Mg-Ca isotopes in carbonate minerals: Insights from first-principles calculations. Geochim. Cosmochim. Acta 208, 185–197.

Wang, W., Zhou, C., Liu, Y., Wu, Z., Huang, F., 2019. Equilibrium Mg isotope fractionation among aqueous Mg^{2+}, carbonates, brucite and lizardite: Insights from first-principles molecular dynamics simulations. Geochim. Cosmochim. Acta 250, 117–129.

Wimpenny, J., Burton, K. W., James, R. H., Gannoun, A., Mokadem, F., Gíslason, S. R., 2011. The behaviour of magnesium and its isotopes during glacial weathering in an ancient shield terrain in West Greenland. Earth Planet. Sci. Lett. 304, 260–269.

Wimpenny, J., Colla, C. A., Yin, Q.-Z., Rustad, J. R., Casey, W. H., 2014. Investigating the behaviour of Mg isotopes during the formation of clay minerals. Geochim. Cosmochim. Acta 128, 178–194.

Wimpenny, J., Gíslason, S. R., James, R. H., Gannoun, A., Pogge von Strandmann, P. A. E., Burton, K. W., 2010. The behaviour of Li and Mg isotopes during primary phase dissolution and secondary mineral formation in basalt. Geochim. Cosmochim. Acta 74, 5259–5279.

Young, E. D., Galy, A., 2004. The isotope geochemistry and cosmochemistry of magnesium. In: Johnson, C. M., Beard, B. L., Albarède, F. (Eds.), Reviews in Mineralogy and Geochemistry. Vol. 55. Mineralogical Society of America, Washington D.C., pp. 197–230.

Table 1: Mg concentration and isotope measurements of the analysed solids and solutions. Concentrations of the residual and exchangeable fractions are given as mg Mg per kg of bulk sample.

Experiment	pH	Temperature °C	solid g	[Mg]$_i$ mg/L initial solution	δ^{26}Mg$_i$ ‰ initial solution	[Mg]$_f$ mg/L final solution	δ^{26}Mg$_f$ ‰ final solution	[Mg]$_e$ g/kg exchangeable Li	δ^{26}Mg$_e$ ‰ exchangeable Li	[Li]$_r$ mg/kg residual Mg and Li	[Mg]$_r$ g/kg residual Mg and Li	δ^{26}Mg$_r$ ‰ residual Mg and Li	f$_e$ mass fraction	f$_r$ mass fraction	[Mg]$_b$ g/kg bulk solid	[Mg]$_b$* g/kg bulk solid	δ^{26}Mg$_b$ ‰ bulk solid	δ^{26}Mg$_b$* ‰ bulk solid	f$_{Mg}$ Mg loss
Reaction vessel - stevensite																			
250117	10.30	20.0	0.242	57.7	0.16	0.1		49.8	0.44	56.7	246.6	0.06	0.17	0.83	181.0	296.4	0.21	0.12	0.00
Bottle - stevensite																			
010217E	10.00	20.0	0.100	47.3	0.14	32.4	0.38	25.9	-0.18	53.5	120.7	-0.71	0.18	0.82	145.5	146.6	-0.61	-0.62	0.68
010217F	10.30	20.0	0.192	46.4	0.03	17.9	0.84	26.9	0.16	33.2	107.3	-0.49	0.20	0.80	144.6	134.2	-0.30	-0.36	0.39
Bottle - stevensite - low Mg series																			
240417B	9.45	20.0	0.004	41.6	0.25	40.1	0.09								107.2		-1.17		0.96
240417J	9.73	20.0	0.039	44.3	-0.01	36.3	0.22	26.9	-0.45	46.8	87.1	-1.05	0.24	0.76	108.7	114.0	-0.91	-0.91	0.82
240417C	9.94	20.0	0.076	41.7	0.02	31.5	0.29	27.2	-0.24	48.7	101.9	-0.85	0.21	0.79	131.0	129.1	-0.85	-0.72	0.75
240417D	10.23	20.0	0.089	42.2	0.22	26.4	0.42	29.7	-0.12	39.2	113.5	-0.67	0.21	0.79	145.3	143.2	-0.67	-0.55	0.63
Bottle - stevensite - high Mg series																			
240417E	8.99	20.0	0.029	436.0	0.08	418.7	0.08	33.2	-0.43	21.1	67.3	-0.97	0.33	0.67	92.6	100.5	-0.78	-0.79	0.96
240417K	9.27	20.0	0.102	447.9	0.02	411.4	0.11	33.3	-0.17	17.3	90.2	-0.91	0.27	0.73	121.6	123.5	-0.77	-0.71	0.92
240417F	9.48	20.0	0.149	433.5	0.04	404.9	0.10	28.3	-0.23	17.4	109.8	-0.79	0.20	0.80	140.1	138.1	-0.71	-0.68	0.93
240417G	9.84	20.0	0.255	457.2	0.16	383.2	0.11	34.8	-0.24	15.5	142.6	-0.52	0.20	0.80	171.8	177.4	-0.47	-0.46	0.84
240417H	10.02	20.0	0.302	422.7	0.12	374.8	0.18	36.4	-0.36	6.4	147.1	-0.27	0.20	0.80	184.4	183.5	-0.33	-0.29	0.89
240417L	10.36	20.0	0.209	438.4	0.04	368.7	0.11	43.9	-0.11	2.4	147.7	-0.37	0.23	0.77	186.8	191.5	-0.27	-0.31	0.84
Reaction vessel - saponite																			
270415	9.00	25.0	0.134	1385	-0.03	1266	0.17								107.1		-0.49		0.91
Bottle - saponite																			
20140624F	9.50	20.0	0.237	830.8	-2.04	764.9	-1.92	26.3	-2.28	15.7	121.7	-2.77	0.18	0.82	142.9	148.0	-2.60	-2.68	0.92
Bottle - saponite - no Li																			
200315C	9.00	19.5	0.022	1296	0.05	1261	0.05	16.7	-0.35		59.9	-0.81	0.22	0.78	76.6	76.6	-0.63	-0.71	0.97
200315D	9.00	19.5	0.020	1263	-0.07	1243	-0.05								79.9		-0.69		0.98
200315E	9.60	19.6	0.059	1300	0.04	1249	0.06	33.4	-0.63		122.8	-0.85	0.21	0.79	155.1	156.2	-0.67	-0.80	0.96
200315F	9.60	19.6	0.071	1229	-0.03	1179	-0.07								150.9		-0.78		0.96
200315G	9.10	35.0	0.013	1222	-0.08	1183	-0.01								157.8		-0.47		0.97
200315H	9.10	50.0	0.070	1168	0.16	1135	0.14								185.8		-0.31		0.97

*Calculated by mass balance

21